Advanced Engineering Materials

ADVANCED ENGINEERING MATERIALS
www.aem-journal.com

RESEARCH ARTICLE OPEN ACCESS

Combined Process- and Phase-Field-Simulation to Predict the Microstructure of Single-Crystal Ni-Based Superalloys

Sean Böhm | André B. Baldissera | Rainer Völkl | Uwe Glatzel

Metals and Alloys, University of Bayreuth, Bayreuth, Germany

Correspondence: Uwe Glatzel (uwe.glatzel@uni-bayreuth.de)

Received: 20 October 2025 | **Revised:** 30 January 2026 | **Accepted:** 2 February 2026

Keywords: Bridgman | dendrite spacing | finite element simulation | Ni-base | phase-field simulation | single crystal

ABSTRACT

A model for the prediction of the dendrite structure in single crystal Ni-based superalloys is established. A combined approach of finite element simulation (FEM) of the temperature conditions during the casting process and phase field simulation of solidification is used to determine the influence of withdrawal rates between 0.5 and 10 mm·min^{-1} on dendrite spacing of CMSX-4 and CM186LC. The model is compared with experimental data from literature, showing good agreement and thus great potential for predicting other parameter sets. Furthermore the influence of wall thicknesses between 0.4 and 2.0 mm was determined for these alloys. The reduction in dendrite spacing with decreasing wall thicknesses can also be predicted by the solidification model. The lack of competition between neighboring dendrites in the volume close to the surface plays a decisive role.

1 | Introduction

Ni-based superalloys are widely used in high-temperature applications like gas turbines and jet engines due to their excellent mechanical properties at high temperatures. The casting of these alloys has evolved over some decades from conventional casting to directional solidification to the casting of single crystals. This development has strongly improved creep properties by eliminating grain boundaries [1–3]. The microstructure of such single-crystal superalloys is usually characterized by the primary dendrite arm spacing λ_P. λ_P is the determining factor for the length scale of microsegregations and therefore has a significant influence on the solution heat treatment [4–6]. In addition, dendrite spacing has a direct influence on mechanical properties because the microsegregations can be reduced by heat treatment but not completely removed [7]. It is well-known, that the dendrite spacing depends on the thermal conditions during solidification [8, 9]. The empirical relationship between temperature gradient G (in K·m^{-1}), solidification rate v_S (in m·s^{-1}), and the primary dendrite arm spacing λ_P (in µm) is therefore as follows, where A (in m$^{0.75}$·K$^{0.5}$·s$^{-0.25}$) is an alloy-dependent constant [10]:

$$\lambda_P = A \cdot v_S^{-0.25} \cdot G^{-0.5} \quad (1)$$

One issue in the research of Ni-based superalloys is the time-consuming and resource-intensive nature of the required experiments. For this reason, modern materials science increasingly relies on simulations to predict how process parameters influence the microstructure of materials. The phase field method is a widely used tool for predicting microstructural evolution in materials research, e.g., in solidification and solid-state transformations [11–13]. This method uses a phase field variable φ calculated as a function of time and position. Each phase that occurs in the simulation is assigned a certain value between 0 and 1 (e.g., in a solidification simulation, 0 corresponds to liquid, and 1 corresponds to solid). The underlying equations for calculating the variable include the thermodynamic driving forces and the diffusion properties of the simulated materials. Previous research has already dealt with phase field simulation of dendritic solidification, particularly of Ni-based superalloys [14–17].

In order to obtain a correlation between the process parameters at the macroscale and the resulting microstructure at the microscale, two simulation methods were combined in this work. In a

first step, a finite element simulation of directional solidification is carried out to determine the temperature conditions during processing. Withdrawal rate and sample wall thickness are the parameters varied in the study. In a second step, the determined temperature conditions are used as input values for the phase field simulations. This work aims to establish a simulation model that can predict microstructures based on casting conditions and alloys. This means that, when new process conditions are developed or new alloys are used, fewer experiments will be required to determine suitable process conditions, saving time and resources. The model was developed using two established alloys.

2 | Simulation Setup

2.1 | Temperature Simulations

The model is calculated with the commercial software COMSOL, simulating the Bridgman process of our lab. It contains the geometric data of the casting samples, the thermophysical data of the used materials, and the thermal boundary conditions of the vacuum induction casting furnace. The model was set up in accordance with the experimental tests carried out at the Institute for Metals and Alloys of the University of Bayreuth [18, 19]. The cast samples consist of a single crystal selector followed by a frame structure with two thin-walled areas (as shown in Figure 1).

Table 1 lists the two series of simulations carried out. The wall thickness of the thin-walled areas was varied to obtain the effect of the geometry. The withdrawal rate varied to obtain the effect of the processing conditions. The parameters used in the simulations are consistent with the geometries and withdrawal rates used in experiments carried out within our group in order to ensure comparability.

Table 2 lists the thermophysical properties of the two Ni-based superalloys CM186LC and CMSX-4 and the material of the shell mold (Al_2O_3), which were used for the simulation. For properties that are temperature dependent, the value at T_L is given as an example.

Figure 1 shows the experimental route of the casting process and the FEM-model of temperature simulation schematically. The ceramic shell mold is manufactured by a positive 3D printed polymer model of Polyvinylbutyral, which is repeatedly dipped into a slurry and subsequently sanded with fused aluminum oxide [18]. The polymer is burned out, and the ceramic shell mold

TABLE 1 | Overview of simulated process parameters.

Varied parameter	Wall thickness in mm	Withdrawal rate in mm·min^{-1}
Withdrawal rate	2.0	0.5, 1.0, 2.0, 3.0, 5.0, 10.0
Wall thickness	0.4, 0.8, 1.2, 2.0	3.0

is sintered. This mold is used to cast metallic samples in the Bridgman process. For the thermophysical properties of the shell, values from previous tests on the ceramic system of the shell molds were used [22]. The thickness of the shell mold is assumed to be constant at 5 mm for all simulations.

Before simulating the Bridgman process, the temperature distribution $T_{dist.}$ in the furnace was measured along the withdrawal direction z. To simulate the withdrawal process, the sample was virtually placed in a temperature field corresponding to the measured temperature distribution. This z-dependent temperature field was then varied over time t (in s), dependent on the withdrawal rate v_w (in m·s^{-1}):

$$T(z,t) = T_{dist.}(z - v_w \cdot t) \quad (2)$$

Figure 2 shows the variation of the temperature field during the simulation schematically. The initial temperature of the sample (including the metal and the ceramic part) is set to match the temperature distribution at the starting time of the simulation, which is equal to the temperature distribution in the Bridgman furnace.

As the process takes place in a vacuum, only thermal radiation is considered for the heat transfer between the temperature field and the surface of the shell mold. In the shell mold, heat transfer was solved exclusively by thermal conduction. In the liquid volumes of the sample, heat convection and heat conduction were used to calculate the heat transfer. By simulating the laminar flow in the liquid volumes of the sample, the contribution of convection was calculated. In the areas that are solidified during the simulation process, the laminar flow was prevented, so there is no convection in these volumes.

Figure 3 shows the division of the mesh into submeshes with different resolutions. The subdivision is made in order to achieve

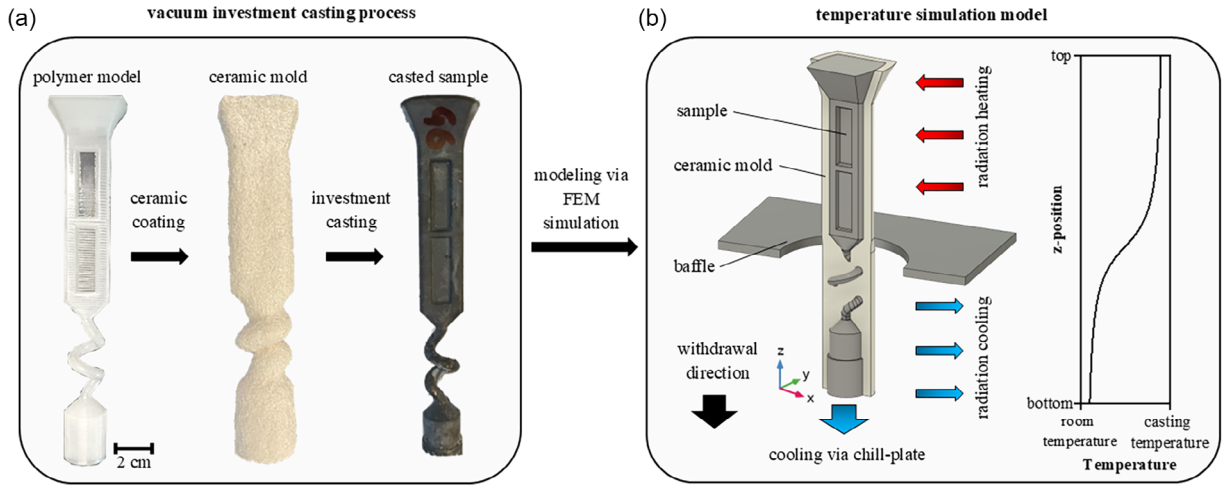

FIGURE 1 | (a) Steps of experimental testing and (b) model for simulation setup.

TABLE 2 | Thermophysical properties used for simulations, marked values (*) are temperature dependent, therefore values at T_L are given as an example.

Thermophysical property	CMSX-4	CM186LC	Al_2O_3
Liquidus temperature T_L in K	1653 [20]	1666 [20]	—
Solidus temperature T_S in K	1593 [20]	1540 [20]	—
Enthalpy of fusion ΔH in kJ·kg^{-1}	240 [20]	190 [20]	—
Density * ρ in kg·m^{-3}	7754 [20]	8147 [20]	1930 [21]
Heat capacity * C_P in J·kg^{-1}·K^{-1}	630 [20]	720 [20]	2500 [21]
Thermal conductivity * k in W·m^{-1}·K^{-1}	24.9 [20]	30.5 [20]	1.15 [21]
Heat transfer coefficient h in W·m^{-2}·K^{-1}	500 [22]	500 [22]	500 [22]
Viscosity * η in Pa·s	0.0084 [23]	0.0077 [24]	—

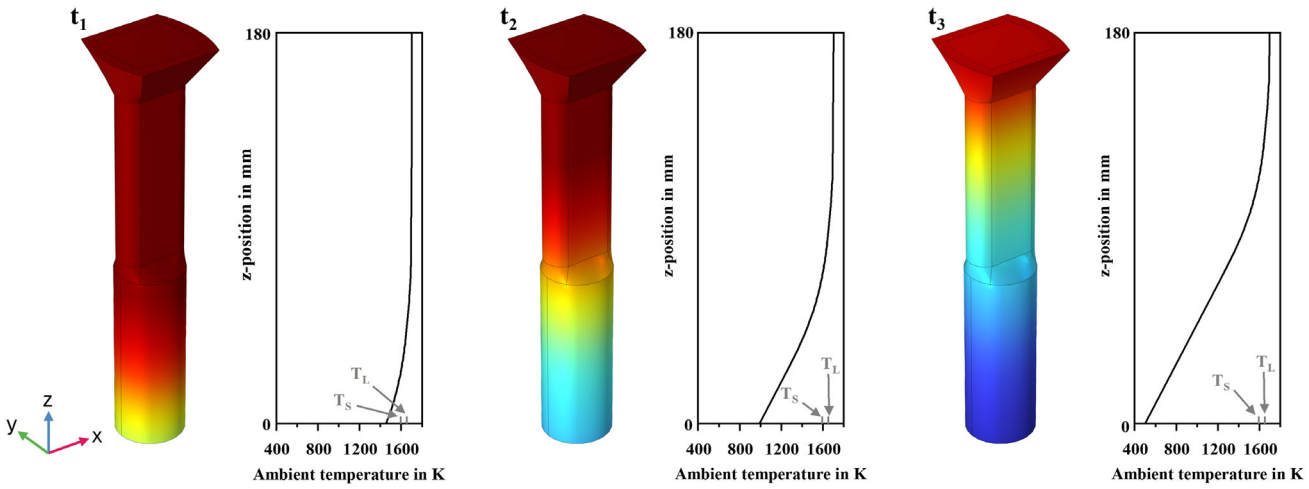

FIGURE 2 | Schematic illustration of the ambient temperature field (T_L and T_S are indicated for CMSX-4) at different times $t_1 < t_2 < t_3$.

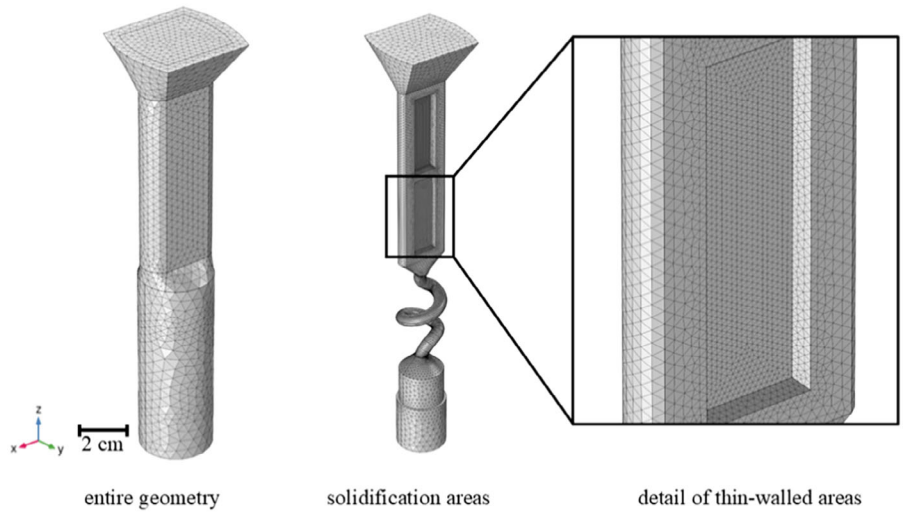

FIGURE 3 | Mesh sizes in the different areas of the simulation.

a good compromise between computation time and accuracy of the results. The shell mold has a coarse mesh with an element size between 0.7 and 9.8 mm. The frame structure of the sample has a mesh with an element size between 0.8 and 2.8 mm. The thin-walled areas have been given a detailed mesh with an element size between 0.009 and 0.5 mm.

2.2 | Microstructure Simulations

A phase field simulation approach is chosen to simulate λ_P for the different solidification conditions. The commercial software MICRESS is used. An approach was used, which considers chemical and interfacial contributions to calculate the phase field

equation. A diffusion solver is also integrated to calculate the concentration field [25]. To provide the required multi-component and multiphase quasiequilibrium conditions, the software was linked to the thermodynamic database TCNI12 via Thermocalc and the mobility database MOBNI6 via DICTRA.

The stored phase-field model is solved by finding the solution to the free energy functional over the domain Ω. This includes the contributions of surface energy density f_{int} and chemical energy density f_{chem}. These depend on the respective local proportion of phases $\{\varphi\}$ (where $\{\varphi\}$ is the fraction of all phases φ_1, φ_2, … φ_n), the number of present phases n, and the local composition c [25].

$$F(\{\varphi\},\vec{c}) = \int_{\Omega} f_{\text{int}}(\{\varphi\}) + f_{\text{chem}}(\{\varphi\},\vec{c}) \tag{3}$$

The change in local composition required to solve the functional is determined using a diffusion solver. Where D is the diffusion matrix of the present phase [25].

$$\dot{\vec{c}} = \nabla \sum_{i=1}^{n} \varphi_i \cdot D_i \cdot \nabla \vec{c}_i \tag{4}$$

Table 3 lists the composition of the used alloys CMSX-4 and CM186LC. These alloys were chosen because they contain 3 wt.% Rhenium. Due to its very low diffusivity, rhenium is prone to pronounced microsegregation and difficult to homogenize during heat treatment. Consequently, the primary dendrite arm spacing plays a crucial role in the resulting microstructural distribution. MAR-M247LC alloy is also included in the table because extensive reference data are available for it, and the geometries and process parameters used in this study have already been experimentally validated in the furnace depicted in the simulation [19].

Figure 4 shows the simulation setup of the phase field model schematically. An approach is chosen that simulates different λ_P by varying the width of the simulation domain. A stable λ_P is then determined using a stability criterion. This is a well-established method that has been used in previous studies to determine λ_P [16, 28]. A single initial seed of the solidified fcc-phase is initially placed in the lower left-hand corner of the simulation domain, whereby the width of the simulation domain is equal to $\lambda_P/2$.

The simulations were performed in two dimensions as a compromise between computational cost and accuracy. Previous studies have shown that reducing a problem from three to two dimensions can significantly decrease simulation time while maintaining high accuracy, provided that the temperature gradient lies within the plane of the simulation domain [29]. It has also been reported that, with respect to predicting λ_P, two-dimensional simulations tend to yield slightly larger spacings than their three-dimensional counterparts [30]. This discrepancy is considered acceptable, since real solidification does not exhibit a single, well-defined dendrite spacing but rather a distribution of spacings.

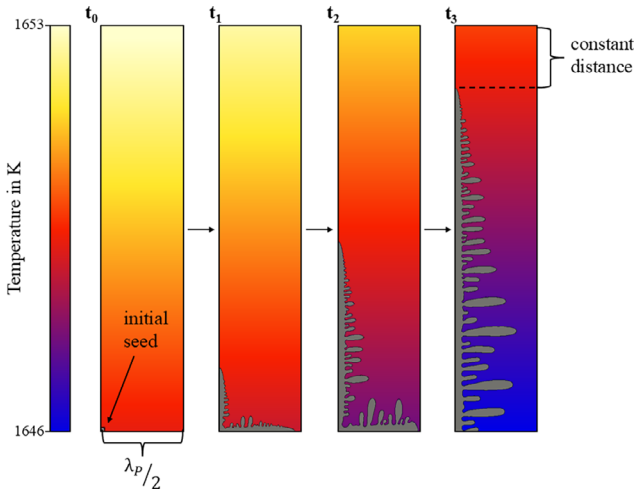

FIGURE 4 | View of the simulation at different time points with temperature in color; areas that have already solidified are shown in gray. CMSX-4 alloy with a withdrawal rate of 5 mm·min^{-1} and a wall thickness of 2 mm.

Moreover, the methodology employed in this work, as described in the Section 3, determines the smallest stable spacing, corresponding to the lower bound of this distribution.

To link the microstructure simulations directly to the process conditions during casting, the microstructure simulation was linked to the FEM simulation. To achieve this, the temperature simulation results were used as input for the solidification temperature conditions. This was achieved by transferring the temperature gradient and cooling rate from the FEM simulation to the phase field simulation domain. A co-moving frame was used to keep the distance from the dendrite tip to the upper boundary of the simulation domain constant. To achieve this, the lower part of the dendrite is pushed downwards out of the simulation domain so that the simulation domain does not become too large. The simulation was performed until a steady state was reached where the temperature at the dendrite tip did not change.

Table 4 lists the range in which the width of the simulation was varied, the height of the two-dimensional simulation domain, and the grid size for different casting conditions. This was adjusted because the resulting process parameters produce dendrite structures of varying fineness. Setting the domain size to these values strikes a reasonable compromise between computing time and accuracy.

A numerical problem in phase-field simulations is the so-called solute trapping. It occurs when the interfacial thickness is not significantly smaller than the diffusion length of the solute elements. As a result, the composition changes from the equilibrium state, leading to an increase in the rate of solidification. It is possible to get rid of this problem by adjusting the value of the

TABLE 3 | Nominal composition of the used alloys in wt.%.

	Ni	Cr	Al	Co	Mo	Ti	Ta	Re	W	Hf
CMSX-4 [26]	60.6 (bal.)	6.5	5.6	9.6	0.6	1.0	6.5	3.0	6.5	0.1
CM186LC [27]	61.5 (bal.)	6.0	5.7	9.2	0.5	0.7	3.5	3.0	8.5	1.4
MAR-M247LC [19]	61.5 (bal.)	8.1	5.7	9.3	0.5	0.7	3.3	0.0	9.4	1.4

TABLE 4 | Parameters of the simulation series.

Wall thickness in mm	Withdrawal rate in mm·min^{-1}	Mesh size in µm	Domain height in µm	Range λ_P in µm	Step size λ_P in µm
2.0	0.5	2.0	1500	120–600	60
2.0	1.0	2.0	1500	120–600	60
2.0	2.0	2.0	1500	120–600	60
0.4, 0.8, 1.2, 2.0	3.0	1.0	1000	100–400	50
2.0	5.0	1.0	1000	100–400	50
2.0	10.0	0.5	800	60–300	40

interface mobility. Interfacial mobility can either be calibrated by comparison with a high-resolution reference simulation [31] or a numerical solidification theory [32]. Due to the shorter computation time, the second approach is chosen. The model by Kurz, Giovanola, and Trivedi (KGT) [33] was selected for the calibration step. The model describes the dendrite tip temperature at a steady state during solidification with a constant temperature gradient and solidification rate. As the model was set up for binary alloys, a pseudo-binary phase diagram is set up for the present case of a multicomponent alloy according to the approach of Böttger et al. [32].

Table 5 lists the calculated temperatures and interface mobilities used in the simulations. In the calibration step, the dendrite tip temperature from the simulation is compared to that of the model. The value of the interface mobility is then adjusted until the two temperatures match. The calibration step was performed on the largest simulated λ_P for each casting condition. The variation of λ_P was then simulated with the same interface mobility for each casting condition.

3 | Results

3.1 | Temperature Simulations

Figure 5 shows the temperature gradient at the liquidus temperature, which is 1666 K for CM186LC and 1653 K for CMSX-4 [20]. To compare the temperature gradients, the center of the thin area was investigated for each simulation. For both alloys, the temperature gradient increases as the withdrawal rate decreases and as the wall thickness decreases. However, the influence of the withdrawal rate is greater than that of the wall thickness. Therefore, the highest temperature gradients occur at a withdrawal rate of 0.5 mm·min^{-1} and a wall thickness of 2 mm (5.17 and 5.43 K·mm^{-1} for CM186LC and CMSX-4, respectively). It is also noticeable that the effect of the variation in the withdrawal rate is more significant for CMSX-4 than for CM186LC. The effect of wall thickness variation is similar for both alloys, but the level of the temperature gradient is slightly lower for CMSX-4 (between 4.48 and 4.81 K·mm^{-1}) than for CM186LC (between 4.61 and 4.93 K·mm^{-1}).

Figure 6 shows the temperature gradient across the isothermal surface in the z and y directions. The temperature gradient in the z direction, which is the solidification direction of the sample, is nearly constant over the entire cross-section for the respective withdrawal rate. The temperature gradient in the y-direction, perpendicular to the surface of the thin-walled areas, on the other hand, is not constant. It is lower in the center of the thin area than at the boundary areas of the sample. It can also be seen that the effect is more pronounced at higher withdrawal rates. However, the magnitude of the temperature gradient in the y-direction is in a significantly smaller range than the temperature gradient in the z-direction.

3.2 | Phase Field Simulations

Figure 7 shows the deviation of the dendrite tip temperature at a steady state from the KGT-temperature [33] for different domain

TABLE 5 | Tip temperature and used interface mobilities for the simulations.

Wall thickness in mm	Withdrawal rate in mm·min^{-1}	CM186LC tip temperature in K	CM186LC interface mobility in 10^{-11} m^4 J^{-1} s^{-1}	CMSX-4 tip temperature in K	CMSX-4 interface mobility in 10^{-11} m^4 J^{-1} s^{-1}
2.0	0.5	1662.83	3.30	1651.45	2.45
2.0	1.0	1661.77	2.66	1650.96	2.67
2.0	2.0	1660.49	3.00	1650.36	3.45
0.4	3.0	1659.50	6.97	1649.91	15.70
0.8	3.0	1659.50	6.58	1649.91	16.43
1.2	3.0	1659.50	6.69	1649.91	16.62
2.0	3.0	1659.50	6.60	1649.91	16.35
2.0	5.0	1658.06	7.85	1649.26	22.80
2.0	10.0	1655.52	7.77	1648.12	11.95

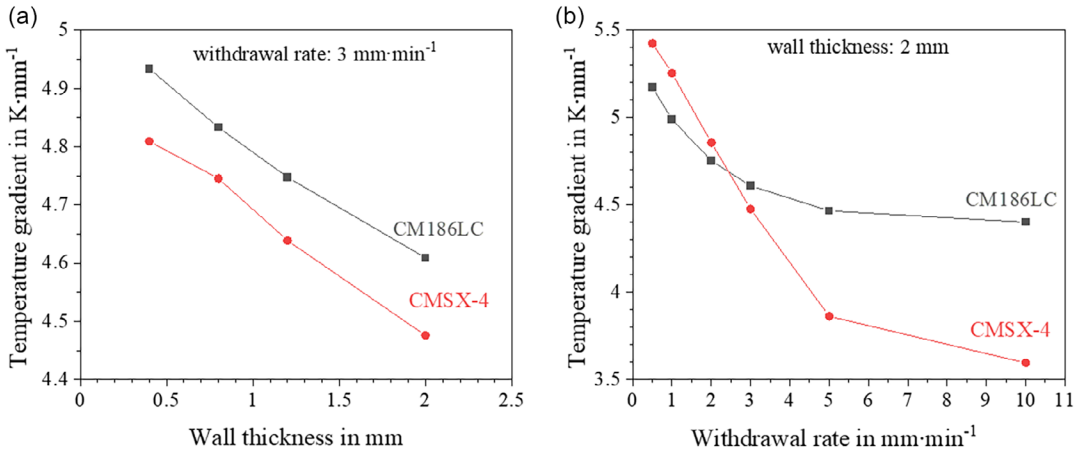

FIGURE 5 | Temperature gradient in the center of the thin-walled area (a) depending on the wall thickness for a constant withdrawal rate of 3 mm·min^{-1}, and (b) dependent on the withdrawal rate for a constant wall thickness of 2 mm.

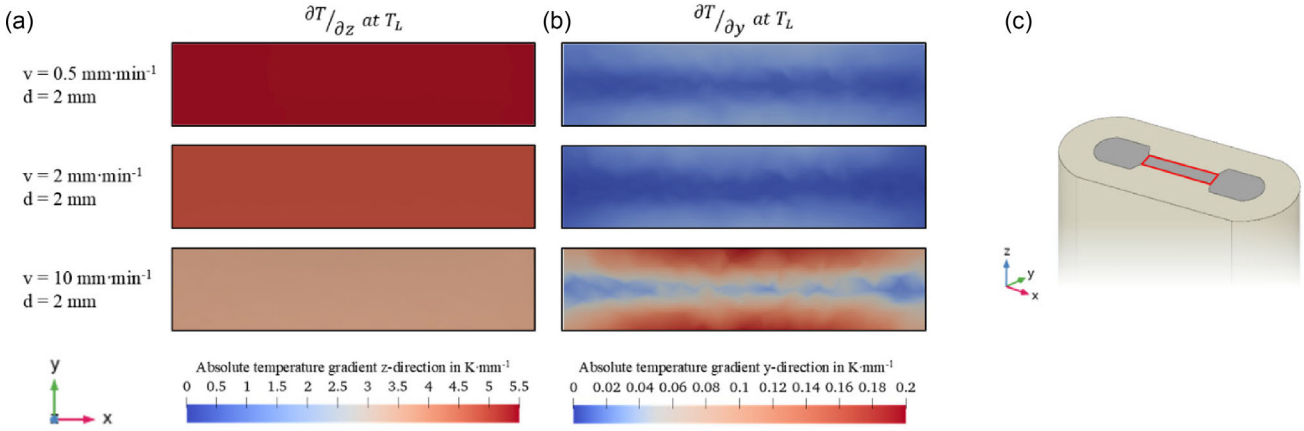

FIGURE 6 | Field of the temperature gradient from the cross-section of the thin-walled area (a) in z-direction and (b) y-direction, for different withdrawal rates at (c) cross-section of the samples, with marked area where the temperature gradients were taken.

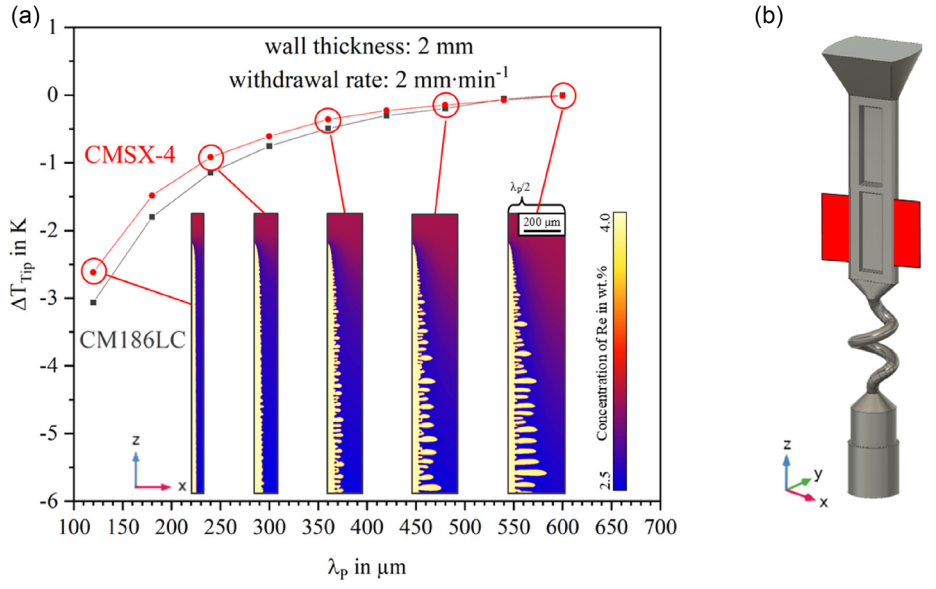

FIGURE 7 | (a) Dendrite tip temperatures and Re-content in the steady state for different λ_P at a withdrawal rate of 2 mm·min^{-1} and a wall-thickness of 2 mm for both alloys, and (b) visualization of the cutting plane.

widths. For the largest domain width, there is no deviation. This is because the simulation was calibrated with this width. With a decreasing domain width, corresponding to a smaller λ_P, the dendrite tip temperature decreases. As there is a temperature gradient in the direction of solidification, the distance of the dendrite tip from the z-position of the KGT temperature increases as the deviation increases. The distance d_{KGT} is calculated from the ratio of the temperature difference ΔT (in K) to the temperature gradient G (in K·m^{-1}). When comparing two dendrites with different λ_P, the tip of the smaller dendrite lies behind the tip of the wider dendrite in the direction of solidification. Another effect to mention is that the distribution of the solutes in the region of the dendrite tip changes with domain width (shown, for example, with the Re content).

Figure 8a shows the concentration field of Re at the dendrite tip in the steady state of the directional solidification simulation for a primary dendrite spacing of 600 µm. The high-melting alloying elements (rhenium in this case) solidify first and segregate mainly in the center of the dendrite. The concentration in the remaining melt decreases accordingly. A concentration gradient is established that decreases from the top of the simulation domain and from the side boundaries of the domain towards the already solidified areas.

Figure 8b shows the distribution of alloying elements at the right boundary of the simulation domain. This boundary is chosen because when comparing two dendrites with different distances, they are placed imaginarily next to each other at this boundary (symmetry line). The dendrites are displaced relative to each other in the direction of solidification, so that this difference needs to be taken into account in the concentration profiles when comparing different spacings.

Figure 8c shows the solutal undercooling at the right domain boundary for the different λ_P. This parameter was used due to the fact that the simulated alloys contain several alloying elements. Therefore, a weighting of the elements and their concentrations is required, which is calculated according to (Equation (5)). The concentration profiles show that the concentration gradient increases with decreasing λ_P.

$$\Delta T_{con} = \sum_k m_{liq}^k \cdot \left(c_{liq}^k - c_{liq}^{k,0}\right) \quad (5)$$

The constitutional undercooling acts as a criterion for deviation from the equilibrium composition of the alloy, where m_{liq} is the liquidus slope at the equilibrium composition, c_{liq} is the local composition, c_{liq}^0 is the equilibrium composition, and k is the alloy element.

To establish a stability criterion for λ_P, two dendrites with different spacings are imaginarily placed side by side at the boundary with the liquid phase. As there are different concentrations of solutes (represented by the constitutional undercooling) at the interface, a gradient is created which acts as a driving force for diffusion. According to the theory of Lu et al. [34] a smaller unit cell gets overgrown if there is a solute flow from a larger neighbor cell. If the solute flow is from the smaller cell to the bigger one, the smaller cell will grow until it is equal to the larger cell. Using the stability criterion, the minimum stable dendrite spacing can be determined.

With increasing absolute constitutional undercooling, and hence increasing deviation from equilibrium composition, there is an increasing driving force for the dendrite to expand its boundaries by solute flow. Since the distribution of elements at the boundary is not homogeneous, the integral of the constitutional undercooling over the boundary length is used. This allows the driving force for the solutal flow to be considered over the entire interface. The λ_P at which the integral of the constitutional undercooling is highest has the greatest driving force to send a solutal flow to its neighbors. Since all smaller dendrites are overgrown, due to the theory of Lu et al. [34], this λ_P represents the minimum of the stable range of primary dendrite spacing.

Figure 9 shows the results of both simulation series. An increase in the withdrawal rate leads to a decrease in λ_P. The range of λ_P reduces from 514 µm at 0.5 mm·s^{-1} to 130 µm at 10 mm·s^{-1} for CMSX-4 and from 432 µm at 0.5 mm·s^{-1} to 124 µm at 10 mm·s^{-1} for CM186LC. A difference in the dendrite spacing of the two alloys is determined. CM186LC has a larger primary dendrite spacing for all parameters used. Compared to CMSX-4 λ_P is

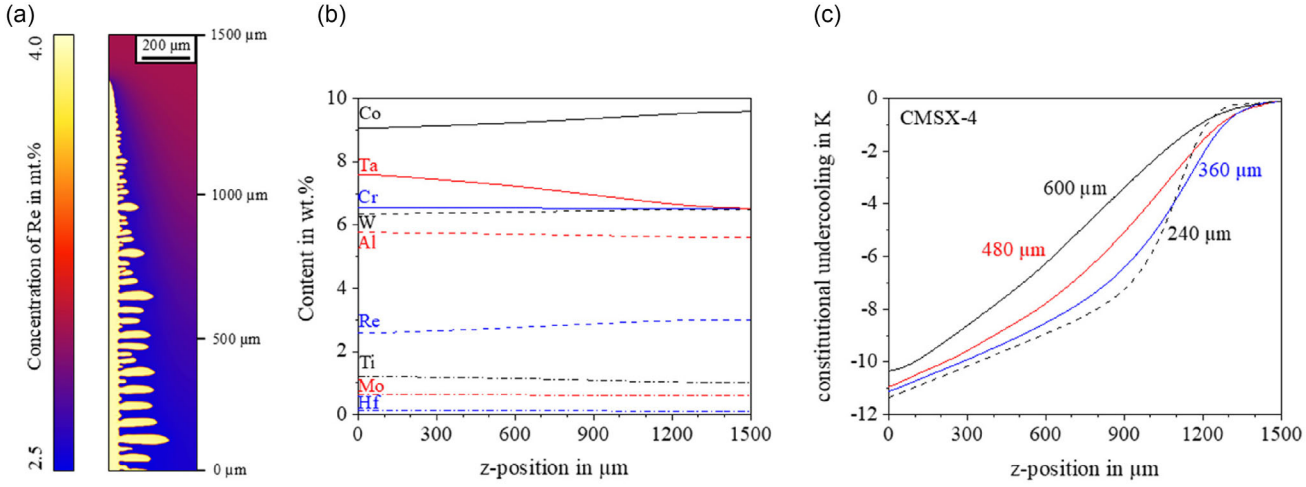

FIGURE 8 | (a) Re- concentration field of the steady state, (b) concentration of alloying elements along the right boundary of the simulation domain, and (c) constitutional undercooling for different λ_P for CMSX-4 with the casting conditions of a withdrawal rate of 2 mm·min^{-1} and a wall thickness of 2 mm.

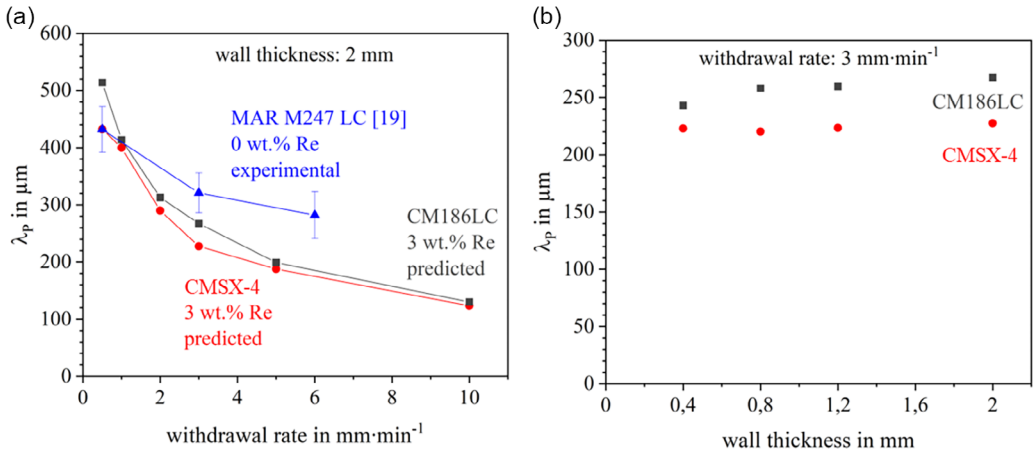

FIGURE 9 | (a) λ_P for withdrawal rates between 0.5 and 10 mm·min^{-1} at a constant wall thickness of 2 mm with experimental data from Körber et al. [19] and (b) for wall thicknesses between 0.4 and 2.0 mm at a constant withdrawal rate of 3 mm·min^{-1}.

up to 82 µm larger. No significant influence on dendrite spacing was observed when wall thickness was varied. The values for λ_P are between 243 and 267 µm for CM186LC and between 220 and 228 µm for CMSX-4. Again, the dendrite spacings are smaller for CMSX-4 than for CM186LC.

4 | Discussion

4.1 | Dependence of the Temperature Gradient on Wall Thickness and Withdrawal Rate

Figure 5 shows that both the withdrawal rate and the wall thickness influence the temperature gradient. In order to understand these results, they are compared with the temperature gradient of the adjacent temperature field. At a Temperature of 1666 K ($T_{liq,CM186LC}$), the measured temperature field of the furnace has a gradient of 6.4 K·mm^{-1}, and at 1653 K ($T_{liq,CMSX-4}$), a gradient of 6.7 K·mm^{-1}. It can be observed that the temperature gradient at the solidification front deviates more and more from the gradient of the external temperature field with increasing withdrawal rate as well as with increasing wall thickness. The decrease in the temperature gradient at higher withdrawal rates can be explained by the fact that the sample has less time to adapt to the external temperature field. This field represents the equilibrium state of temperature that the sample would assume with a long residence time. By changing the external temperature field more quickly, the sample deviates more from the equilibrium state, and the temperature gradient is reduced. The decrease in temperature gradient with increasing wall thickness can also be explained by the nonadaptation of the equilibrium state. As the wall thickness increases, the heat capacity of the sample increases, and therefore, more energy is stored in the form of heat. It therefore takes longer for the sample temperature to equal the temperature of the external field, and the gradient decreases. With increasing deviation from the equilibrium temperature field, and consequently a larger temperature difference between the melt and the external temperature, natural convection is enhanced. Larger temperature gradients can therefore be compensated more rapidly by the intensified convective transport, which partially counteracts the effect described above. As a result, the curve flattens at very high cooling rates.

Looking at the contributions of the temperature gradients $\partial T/\partial z$ and $\partial T/\partial y$ (Figure 6), the main direction of the temperature gradient is, as expected, the z-direction (direction of solidification). The differences in the temperature gradient in the y-direction are significantly less than the temperature gradient in the z-direction. Even the differences in temperature gradient in the z-direction due to variation in wall thickness and withdrawal rate are higher than the absolute values of the temperature gradients in the y-direction. We therefore conclude that the influence of the process parameters, like withdrawal rate and external temperature gradient, during dendritic solidification is significantly greater than the local differences in temperature gradients due to sample geometry down to thicknesses of 0.4 mm.

4.2 | Influence of Wall Thickness on Dendrite Growth

Figure 9 shows the influence of the withdrawal rate, which is significantly higher than the influence of the wall thickness. This behavior can be attributed to two main factors. First, variations in the withdrawal rate lead to significantly larger changes in the temperature gradient than variations in the wall thickness. Second, according to (Equation (1)), the solidification rate is a key parameter in dendrite formation. While the solidification rate is directly affected by the withdrawal rate, it is only weakly influenced by changes in wall thickness alone. It can also be seen that the simulated dendrite spacing for different withdrawal rates shows good agreement with experimental results from Körber et al. [19] for MAR-M247 LC. The simulated dendrite spacing tends to be smaller than the experimental spacing. The results with which the simulation was compared were carried out on the same furnace [19]. Therefore, the temperature conditions during casting are comparable. The small deviations in the simulation are due to two factors. On the one hand, in the experimental data, MAR-M247 LC was used [19]. In contrast to CMSX-4 and CM186LC, this alloy does not contain Re. An increased Re content has been demonstrated to result in a reduction in dendrite spacing in Ni-based alloys [35, 36], a phenomenon that may provide a rationale for the observed discrepancies between experimental and simulated results. On the other hand, the method used in the simulation determines the smallest stable dendrite

spacing. However, since there is no specific stable spacing for a solidification state, but rather a stable range, the experimental average spacing is larger. However, when the simulation series for different wall thicknesses was also compared with experimental data from Körber et al. [19], a discrepancy became apparent.

It is necessary to look at the difference between the solidification in bulk volume and in the vicinity of the metal surface. As already experimentally observed [19], there is a difference in λ_P between these two regions. λ_P is for a constant withdrawal rate within a small range in bulk volume, independent of the wall thickness. The dendrite spacing in volumes close to the surface is lower than in the bulk volume. Because the influence of the interface area is greater on thin samples, a decrease in the wall thickness leads to a decrease in the mean dendrite spacing of the entire sample. The mean λ_P can be described by (Equation (6)), dependent on the dendrite spacing in the bulk area $\lambda_{P,\,bulk}$ (in µm), the dendrite spacing in the interface region $\lambda_{P,\,int}$ (in µm), the thickness of the area with reduced dendrite spacing d_{int} (in mm), and the wall thickness d (in mm):

$$\bar{\lambda}_P = \frac{2d_{int} \cdot \lambda_{P,int} + (d - 2d_{int}) \cdot \lambda_{P,bulk}}{d} \tag{6}$$

Figure 10 shows a closer look at the comparison between the bulk and interface regions of dendrite growth. There is a difference in diffusion between the dendrites and their neighbors in these regions. While a dendrite in the bulk material has to compete with four neighbors for solutes, a dendrite at the boundary only has to compete with three neighbors. According to Lu's theory [34], which states that a smaller dendrite will be overgrown if there is a flow of solutes from a larger neighbor, a dendrite at the boundary cannot be overgrown from the side of the metal surface. The theoretical minimum value for the dendrite spacing perpendicular to the interface is therefore half the dendrite spacing from the bulk material. The dendrite spacing parallel to the interface is not affected by this effect and therefore remains the same. This model agrees with experimental results [19], where a directional dependence of dendrite spacing at the boundaries is observed.

The anisotropic growth behavior of the dendrites in the vicinity of the metal surface results in an average dendrite spacing of 0.71 $\lambda_{P,\,bulk}$, and a thickness of the edge area with smaller dendrite spacings of 0.5 $\lambda_{P,\,bulk} = d_{int}$. The following relationship can therefore be established for the average dendrite spacing as a function of wall thickness and primary dendrite spacing in bulk volumes:

$$\bar{\lambda}_P = \begin{cases} \sqrt{\frac{d}{2} \cdot \lambda_{P,bulk}} & \text{for } d < \lambda_{P,bulk} \\ \dfrac{\lambda_{P,bulk} \cdot \left(d - 0.29 \cdot \lambda_{P,bulk}\right)}{d} & \text{for } d \geq \lambda_{P,bulk} \end{cases} \tag{7}$$

Figure 11 shows an example of this relationship for primary dendrite spacings in bulk volumes of 100, 200, and 300 µm. The influence of wall thickness plays a major role for small wall thicknesses, while for larger wall thicknesses the value of the average dendrite spacing approaches that of the bulk dendrite spacing. A similar trend was also observed in experimental studies [19, 37].

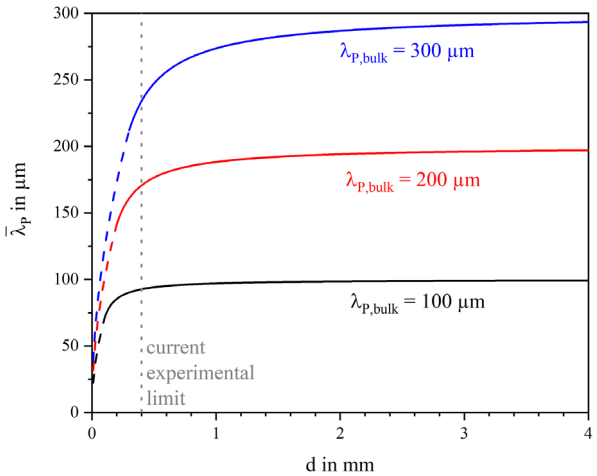

FIGURE 11 | Dependence of the mean dendrite spacing on the wall thickness, exemplary for dendrite spacings in the bulk of 100, 200, and 300 µm.

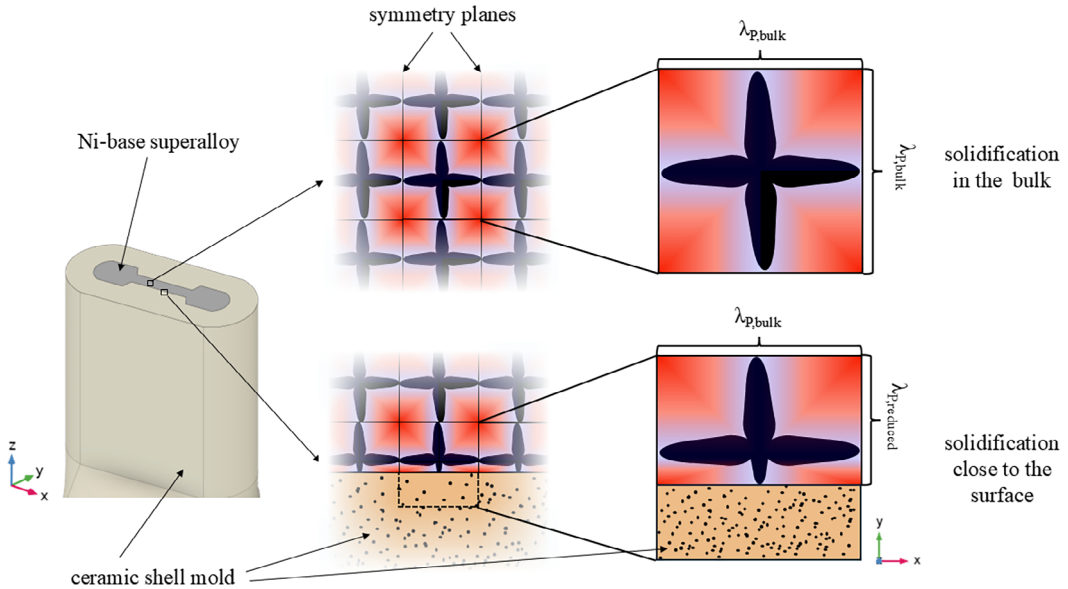

FIGURE 10 | Schematic illustration of the λ_P and the neighborhood relations between the dendrites close to the metal surface and in the bulk material.

5 | Conclusion

Our model predicts the microstructure during direct solidification of Ni-based superalloys using a combined approach of finite element (FEM) and phase field simulation. This approach makes it possible to estimate the microstructure and determine the influence of process parameters and geometry. The parameter ranges considered in this study (wall thicknesses of 0.4–2.0 mm and withdrawal rates of 0.5–10.0 mm/min) can be readily extended as desired, and the investigated alloy systems can likewise be adapted, provided that the required thermophysical and thermodynamic material data are available.

- The temperature simulations show a dependence of the temperature gradient on withdrawal rate and wall thickness. The influence of the withdrawal rate is stronger.
- The microstructural simulation of the dendrite spacing at different withdrawal rates shows agreement with experimental results.
- The effect of the wall thickness on dendrite spacing is more pronounced in volumes close to the surface. The width of this volume is half the primary dendrite spacing in bulk volume. A model has been established that describes a reduced dendrite spacing in this region due to the lack of competition for dendrite growth from one side.
- As volumes close to the surface of thin specimens occupy a larger proportion of the total cross-section, the influence increases with decreasing wall thickness. The influence also increases with increasing $\lambda_{P,\,bulk}$. For $\lambda_{P,\,bulk} = 300\,\mu m$, a significant decrease in the mean primary dendrite spacing is observed for a wall thickness of ≤ 0.8 mm.

Acknowledgments

We gratefully acknowledge financial support by the German Research Foundation (DFG) with project 515779084 – GL181/70−1.

Open Access funding enabled and organized by Projekt DEAL.

Funding

This study was supported by Deutsche Forschungsgemeinschaft (515779084).

Data Availability Statement

The data that support the findings of this study are available from the corresponding author upon reasonable request.

References

1. R. C. Reed, *The Superalloys* (Cambridge University Press, 2009).

2. H. Long, S. Mao, Y. Liu, Z. Zhang, and X. Han, "Microstructural and Compositional Design of Ni-Based Single Crystalline Superalloys — A Review," *Journal of Alloys and Compounds* 743 (2018): 203–220.

3. T. M. Pollock and S. Tin, "Nickel-Based Superalloys for Advanced Turbine Engines: Chemistry, Microstructure and Properties," *Journal of Propulsion and Power* 22, no. 2 (2006): 361–374.

4. H. T. Pang, N. D'Souza, H. Dong, H. J. Stone, and C. M. F. Rae, "Detailed Analysis of the Solution Heat Treatment of a Third-Generation Single-Crystal Nickel-Based Superalloy CMSX-10K," *Metallurgical and Materials Transactions A* 47, no. 2 (2016): 889–906.

5. G. E. Fuchs, "Solution Heat Treatment Response of a Third Generation Single Crystal Ni-Base Superalloy," *Materials Science and Engineering* A300 (2001): 52–60.

6. A. Szczotok and B. Chmiela, "Effect of Heat Treatment on Chemical Segregation in CMSX-4 Nickel-Base Superalloy," *Journal of Materials Engineering and Performance* 23, no. 8 (2014): 2739–2747.

7. S. Tian, C. Zhang, X. Yu, Z. Zeng, and Y. Su, "Influence of Withdrawing Rates on Elements Segregation and Creep Properties of A Single Crystal Nickel-Based Superalloy," *High Temperature Materials and Processes* 31, no. 2 (2012): 7–13.

8. H. Dong, W. Wang, and P. D. Lee, "Simulation of the Thermal History Dependence of Primary Spacing During Directional Solidification," *Superalloys* 2004 (2004): 925–931.

9. M. Dexin and P. R. Sahm, "Primary Spacing in Directional Solidification," *Metallurgical and Materials Transactions A* 29 (1998): 1113–1119.

10. D. Goldschmidt, "Einkristalline Gasturbinenschaufeln Aus Nickelbasis-Legierungen. Teil I: Herstellung Und Mikrogefüge," *Materialwissenschaft und Werkstofftechnik* 25 (1994): 311–320.

11. R. S. Qin and H. K. Bhadeshia, "Phase Field Method," *Materials Science and Technology* 26, no. 7 (2010): 803–811.

12. B. Nestler and A. Choudhury, "Phase-Field Modeling of Multi-Component Systems," *Current Opinion in Solid State and Materials Science* 15, no. 3 (2011): 93–105.

13. I. Steinbach, "Phase-Field Models in Materials Science," *Modelling and Simulation in Materials Science and Engineering* 17, no. 7 (2009): 073001.

14. N. Warnken, D. Ma, A. Drevermann, R. C. Reed, S. G. Fries, and I. Steinbach, "Phase-Field Modelling of as-Cast Microstructure Evolution in Nickel-Based Superalloys," *Acta Materialia* 57, no. 19 (2009): 5862–5875.

15. C. Yang, Q. Xu, and B. Liu, "Primary Dendrite Spacing Selection during Directional Solidification of Multicomponent Nickel-Based Superalloy: Multiphase-Field Study," *Journal of Materials Science* 53, no. 13 (2018): 9755–9770.

16. B. Böttger, A. Seiz, R. Sowa, R. Berger, and M. Apel, "Numerical Prediction of Primary Dendrite Arm Spacing (PDAS), Properties of the Mushy Zone, and Freckle Risk for Various Multicomponent Ni-Base Superalloys Using the 3D-Phase-Field Method," *Computational Materials Science* 236 (2024): 112854.

17. M. Fleck, F. Querfurth, and U. Glatzel, "Phase Field Modeling of Solidification in Multi-Component Alloys with a Case Study on the Inconel 718 Alloy," *Journal of Materials Research* 32, no. 24 (2017): 4605–4615.

18. S. Körber, R. Völkl, and U. Glatzel, "3D Printed Polymer Positive Models for the Investment Casting of Extremely Thin-Walled Single Crystals," *Journal of Materials Processing Technology* 293 (2021): 117095.

19. S. Körber, M. Fleck, R. Völkl, and U. Glatzel, "Anisotropic Growth of the Primary Dendrite Arms in a Single-Crystal Thin-Walled Nickel-Based Superalloy," *Advanced Engineering Materials* 24, no. 6 (2022): 2101332.

20. P. N. Quested, R. F. Brooks, L. Chapman, R. Morrell, Y. Youssef, and K. C. Mills, "Measurement and Estimation of Thermophysical Properties of Nickel Based Superalloys," *Materials Science and Technology* 25, no. 2 (2009): 154–162.

21. M. Xu, S. N. Lekakh, and V. L. Richards, "Thermal Property Database for Investment Casting Shells," *International Journal of Metalcasting* 10, no. 3 (2016): 329–337.

22. C. H. Konrad, M. Brunner, K. Kyrgyzbaev, R. Völkl, and U. Glatzel, "Determination of Heat Transfer Coefficient and Ceramic Mold Material Parameters for Alloy IN738LC Investment Castings," *Journal of Materials Processing Technology* 211, no. 2 (2011): 181–186.

23. E. Ricci, D. Giuranno, R. Novakovic, et al., "Density, Surface Tension, and Viscosity of CMSX-4 Superalloy," *International Journal of Thermophysics* 28, no. 4 (2007): 1304–1321.

24. K. C. Mills, Y. M. Youssef, Z. Li, and Y. Su, "Calculation of Thermophysical Properties of Ni-Based Superalloys," *ISIJ International* 46 (2006): 623–632.

25. J. Eiken, B. Böttger, and I. Steinbach, "Multiphase-Field Approach for Multicomponent Alloys with Extrapolation Scheme for Numerical Application," *Physical Review E* 73, no. 6 (2006): 66122.

26. K. Harris and J. B. Wahl, "Improved Single Crystal Superalloys, CMSX-4(SLS)[La+Y] and CMSX-486," *Superalloys* 2004 (2004): 45–52.

27. R. J. Quigg, "New Alloy Developments in Single Crystal and DS Alloys," *High Temperature Materials and Processes* 11 (1993): 247–254.

28. Z. Wang, J. Li, J. Wang, and Y. Zhou, "Phase Field Modeling the Selection Mechanism of Primary Dendritic Spacing in Directional Solidification," *Acta Materialia* 60, no. 5 (2012): 1957–1964.

29. N. S. Bailey, K.-M. Hong, and Y. C. Shin, "Comparative Assessment of Dendrite Growth and Microstructure Predictions during Laser Welding of Al 6061 via 2D and 3D Phase Field Models," *Computational Materials Science* 172 (2020): 109291.

30. J. Lee, M. Ohno, Y. Shibuta, and T. Takaki, "Uniquely Selected Primary Dendrite Arm Spacing during Competitive Growth of Columnar Grains in Al–Cu Alloy," *Journal of Crystal Growth* 558 (2021): 126014.

31. B. Böttger, M. Apel, B. Santillana, and D. G. Eskin, "Relationship Between Solidification Microstructure and Hot Cracking Susceptibility for Continuous Casting of Low-Carbon and High-Strength Low-Alloyed Steels: A Phase-Field Study," *Metallurgical and Materials Transactions A* 44, no. 8 (2013): 3765–3777.

32. B. Böttger, C. Haberstroh, and N. Giesselmann, "Cross-Permeability of the Semisolid Region in Directional Solidification: A Combined Phase-Field and Lattice-Boltzmann Simulation Approach," *JOM* 68, no. 1 (2016): 27–36.

33. W. Kurz, B. Giovanola, and R. Trivedi, "Theory of Microstructural Development during Rapid Solidification," *Acta Metallurgica* 34 (1986): 823–830.

34. S.-Z. Lu and J. D. Hunt, "A Numerical Analysis of Dendritic and Cellular Array Growth: The Spacing Adjustment Mechanisms," *Journal of Crystal Growth* 123 (1992): 17–34.

35. Z. H. Tan, X. G. Wang, L. H. Ye, et al., "Effects of Rhenium on the Microstructure and Creep Properties of Novel Nickle-Based Single Crystal Superalloys," *Materials Science and Engineering: A* 761 (2019): 138042.

36. Z. Liu, M. Li, F. Wang, Q. Yang, D. Li, and D. Ma, "Effects of Rhenium and High-Angle Grain Boundaries upon the Elemental Distribution and Microstructure of Ni-Based Single-Crystal Superalloys," *Materials Characterization* 196 (2023): 112655.

37. H. Xu, T. Huang, C. Ai, C. Zhang, J. Zhang, and L. Liu, "Effect of Thickness on Microstructure of Thin-Walled Nickel-Based Single-Crystal Superalloy Castings," *Journal of Materials Research and Technology* 29 (2024): 2912–2917.